Through-Layer Buckle Wavelength-Gradient Design for the Coupling of High Sensitivity and Stretchability in a Single Strain Sensor

Tengyu He,[†,§] Chucheng Lin,[‡] Liangjing Shi,[†] Ranran Wang,*,[†] and Jing Sun*,[†]

[†]State Key Laboratory of High Performance Ceramics and Superfine Microstructure and [‡]Analysis and Testing Center for Inorganic Materials, Shanghai Institute of Ceramics, Chinese Academy of Sciences, Shanghai 200050, China

[§]University of Chinese Academy of Sciences, 19(A) Yuquan Road, Beijing 100049, China

Ⓢ Supporting Information

ABSTRACT: Recent years have witnessed a breathtaking development of wearable strain sensors. Coupling high sensitivity and stretchability in a strain sensor is greatly desired by emerging wearable applications but remains a big challenge. To tackle this issue, a through-layer buckle wavelength-gradient design is proposed and a facile and universal fabrication strategy is demonstrated to introduce such a gradient into the sensing film with multilayered sensing units. Following this strategy, strain sensors are fabricated using graphene woven fabrics (GWFs) as sensing units, which exhibit highly tunable electromechanical performances. Specifically, the sensor with 10-layer GWFs has a gauge factor (GF) of 2996 at a maximum strain of 242.74% and an average GF of 327. It also exhibits an extremely low minimum detection limit of 0.02% strain, a fast signal response of less than 90 ms, and a high cyclic durability through more than 10 000 cycling test. Such excellent performances qualify it in accurately monitoring full-range human activities, ranging from subtle stimuli (e.g., pulse, respiration, and voice recognition) to vigorous motions (finger bending, walking, jogging, and jumping). The combination of experimental observations and modeling study shows that the predesigned through-layer buckle wavelength gradient leads to a layer-by-layer crack propagation process, which accounts for the underlying working mechanism. Modeling study shows a great potential for further improvement of sensing performances by adjusting fabrication parameters such as layers of sensing units (n) and step pre-strain (ε_{sp}). For one thing, when ε_{sp} is fixed, the maximum sensing strain could be adjusted from >240% ($n = 10$) to >450% ($n = 15$) and >1200% ($n = 20$). For the other, when n is fixed, the maximum sensing strain could be adjusted from >240% ($\varepsilon_{sp} = 13.2\%$) to >400% ($\varepsilon_{sp} = 18\%$) and >800% ($\varepsilon_{sp} = 25\%$).

KEYWORDS: stretchable, wearable, strain sensor, graphene, gradient, buckle, crack
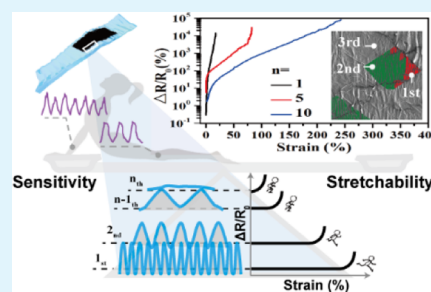
1. INTRODUCTION

Stretchable strain sensors that could detect strain variations and respond with electrical signals have attracted considerable research efforts because of their promising applications in the electronic skin,[1,2] intelligent human/machine interactions,[3,4] disease diagnosis,[5,6] and personal health care,[7,8] and so forth. The past decade has witnessed exhilarating success in improving the flexibility and stretchability of strain sensors either by designing special geometries for conventional materials or by using novel conductive materials,[9] such as metal nanoparticles,[10,11] metal nanowires,[12,13] semiconductor nanowires,[14,15] carbon nanotubes (CNTs),[16−19] graphene,[20−24] and carbon black (CB).[25,26] Wearable applications require strain sensors to be highly flexible and stretchable and sufficiently sensitive so that they could accommodate and detect full-range human activities, ranging from subtle physiological activities such as breathing, heartbeat, and the pulse to mild facial muscle motion and vigorous bending and rotation of joints (hands, arms, legs, and spinal). Despite such progress, the majority of reported strain sensors either have high stretchability (indicated by the maximum sensing strain, ε) but low sensitivity (indicated by the gauge factor, GF)[16,26−33] or the opposite.[15,17,34−42] In other words, attaining high

stretchability and sensitivity simultaneously still remains a big challenge. Some of the recent studies[20,21,43−49] have shown strain sensors with a relatively balanced combination of stretchability and sensitivity. For instance, Yin et al.[50] have recently reported a strain sensor based on reduced graphene oxide (rGO) woven fabrics prepared from pyrolyzing commercial cotton bandages coated with graphene oxide (GO) sheets, which has a combination of relatively large stretchability (57%) and a high sensitivity (GF = 416, 0−40% strain). Still, a further improvement in both the stretchability and sensitivity should be greatly favored by emerging wearable applications.

The dilemma lies in that the stretchability and sensitivity are a pair of mutually exclusive properties: on one hand, a wide sensing range requires the integrity of the conducting network under a large deformation. On the other, high sensitivity is originated from drastic structural changes even under subtle strain. At the first glance, a compromise between these two desirable but contradictory properties seems to be impossible.
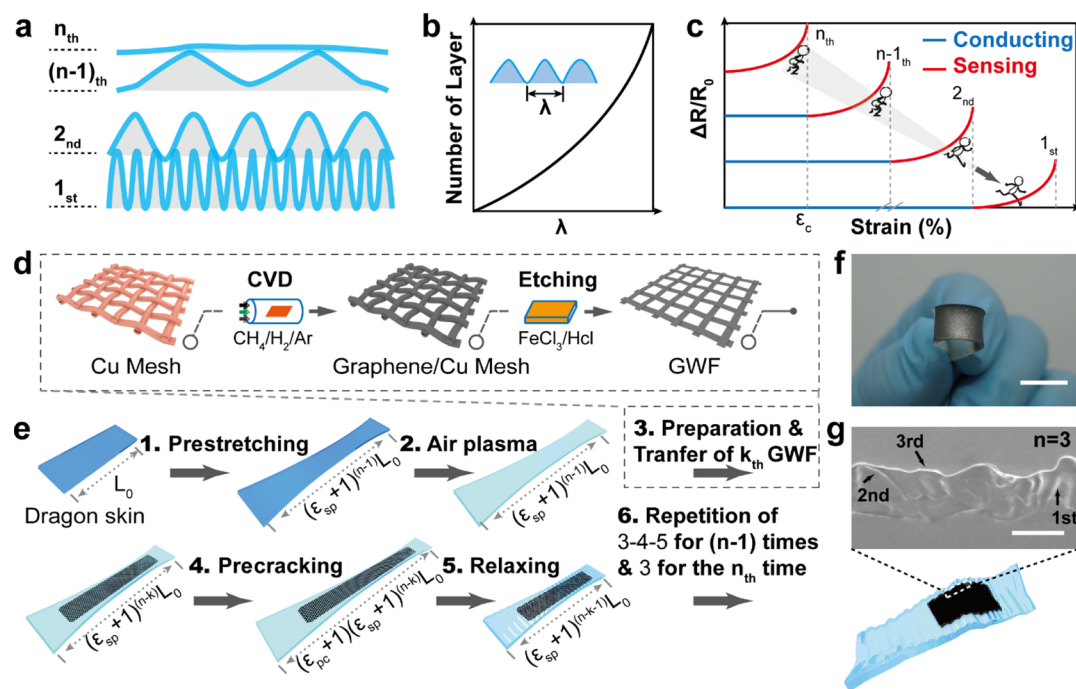
Figure 1. Schematic illustration of the fundamental design philosophy, fabrication strategy, and SEM characterization of the MBGWF sensing film. Schematic illustration of (a) structure design of *n*-layered sensing units with a through-layer buckle wavelength gradient, (b) buckle wavelength gradient curve through layers [the inset image shows the definition of buckle wavelength (λ)], (c) prediction of electromechanical performances of individual sensing units shown in (a), (d) preparation of the GWF, and (e) fabrication of the MBGWF sensing film. (f) Photograph of the MBGWF sensing film with *n* = 10. Scale bar, 2 cm. (g) Cross-sectional SEM image of the MBGWF sensing film with *n* = 3. Different layers were pointed out by arrows. Scale bar, 3 μm.

Fortunately, in nature, exist abundant inspirations for such an integration.[51−55] Take the compromise between stiffness and softness, for example. In adhesive tarsal setae of ladybird beetle, a stiffness gradient is created by the gradual decrease of the proportion of the elastic protein resilin from tips of setae to their bases, endowing the setae with an effective adaption to rough surfaces while preventing lateral collapse.[52,53] In a similar way, the squid beak protects itself from damage while preying.[54,55] In both cases, the local stiffness is adapted by a stiffness gradient to reach a global compromise between stiffness and softness. These findings suggest that achieving both a high strain sensing range and sensitivity is possible if we could adapt the gradient concept to the design of a graded structure, in which the local mechanical property is differentiated such that specific local parts are immune to structural changes, whereas others are sensitive to such changes.

In this work, we proposed a through-layer buckle wavelength (λ) gradient design and provided a facile and universal strategy for the fabrication of corresponding sensing film. As a demonstration, the graphene woven fabrics (GWFs) were used as the sensing units. The GWFs were multilayered and selectively buckled (MBGWF), in which the buckle wavelength of GWFs increases from the bottom layer to the top. MBGWF strain sensors with varying fabrication parameters exhibit highly tunable maximum sensing strain (12 to 242.74%) and sensitivity (maximum GF varying from 105 674 to 2996). Particularly, the 10-layer MBGWF strain sensor demonstrates an optimization both in the sensitivity (maximum GF = 2996) and in the strain sensing range (up to 242.74%), which is 23 times higher than that of a single-layer GWF-based strain sensor previously reported.[38] Meanwhile, the incorporation of the ultralow minimum detection limit (0.02%), a fast signal

response (<90 ms), and a high cyclic durability (>10 000 cycles) qualifies this strain sensor in accurately monitoring full-range human activities, ranging from subtle stimuli (e.g., pulse, respiration, and voice recognition) to vigorous motions (finger movement, walking, jogging, and jumping). Further experimental observations revealed that the underlying working mechanism is a layer-by-layer crack propagation process, based on which a mathematical model was developed to study effects of critical fabrication parameters on electromechanical performances.

2. EXPERIMENTAL SECTION

2.1. Preparation of the GWF. The copper mesh (wires ~100 μm in diameter and meshes ~150 μm in width, Figure S5) was cut into pieces of 6 × 8 cm^2 and ultrasonically treated with hydrochloric acid and acetone to clean the surface and remove the thin oxide layer. The treated copper mesh was put into a quartz tube with flowing gas mixture (Ar/H$_2$ = 1000:100 mL min^{-1}) and heated to 1000 °C (a heating rate of 16.67 °C min^{-1}) and annealed at 1000 °C for 30 min. Then, the gas mixture was adjusted to Ar (400 mL min^{-1}) and H$_2$ (45 mL min^{-1}), and CH$_4$ (40−60 mL min^{-1}) was introduced into the tube at an ambient pressure. After growth of 25 min, the tube was rapidly cooled down to 18 °C. The copper mesh deposited with graphene was cut into pieces of L × 8 mm^2 (L depends on the fabrication parameters and the final size of the MBGWF sensing film. See Table S5 for details) and put onto the etchant solution of FeCl$_3$ (0.5 mol L^{-1}) and HCl (0.5 mol L^{-1}) to etch the copper mesh. The as-prepared free-standing GWF on the solution was rinsed thoroughly by replacing the etchant solution with deionized water.

2.2. Fabrication of the MBGWF Strain Sensor with a Buckle Wavelength Gradient. Dragon Skin (10 Medium, Smooth-On inc.) of 60 mm × 15 mm × 1 mm was prepared by mixing agents A and B (1:1 in weight) thoroughly and curing at 80 °C for 120 min. The Dragon Skin was prestretched to the length of $(\varepsilon_{sp} + 1)^{(n-1)}L_0$ (L_0 = 6 cm) and treated by glow discharge plasma [air plasma (AP), 50 Pa,
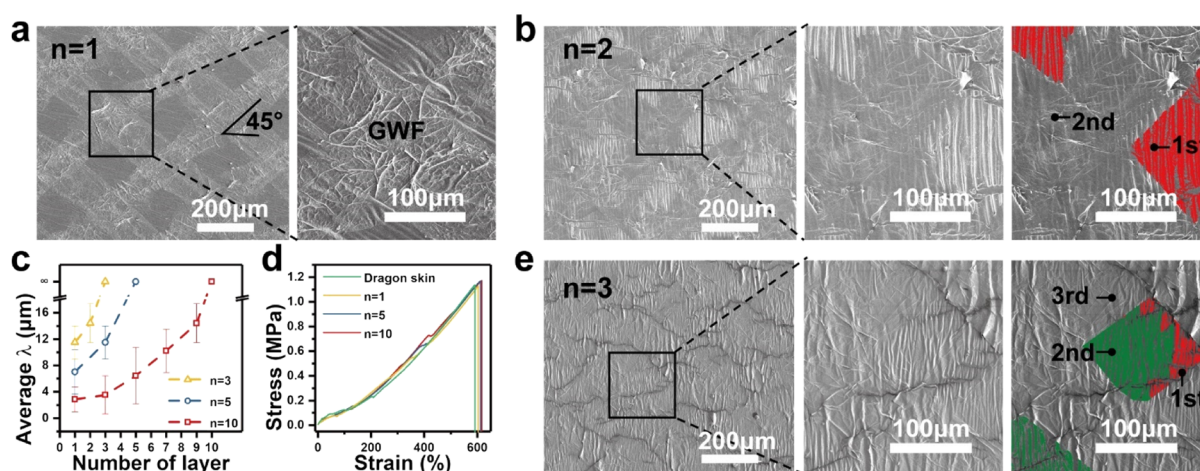
Figure 2. Characterization of the buckle wavelength gradient and mechanical properties of the MBGWF sensors. SEM image and corresponding enlarged view of the MBGWF sensing film with (a) $n = 1$, (b) $n = 2$, and (e) $n = 3$. Colorization was achieved using image analysis software (see Supporting Information for details). (c) Through-layer buckle wavelength gradient curves of the MBGWF sensing film with varying n values. (d) Stress vs strain curves for the Dragon skin and MBGWF sensors with varying n values.

100 W, 5 min]. Afterward, the as-prepared GWF was directly transferred onto the Dragon Skin from water and dried at 80 °C for 20 min (transfer step). The transfer process was carefully controlled such that the stretching angle [the included angle between each graphene microribbon (GMR) and the desired stretching direction] was 45° (Figure 2a). The as-transferred GWF was pre-cracked and buckled by stretching the substrate to the length of $(\varepsilon_{pc} + 1)(\varepsilon_{sp} + 1)^{(n-k)}L_0$ (pre-cracking step) and then relaxed (relaxing step) to the length of $(\varepsilon_{sp} + 1)^{(n-k-1)}L_0$. Last, by repeating the transfer, precracking, and relaxing step $(n - 1)$ times and the transfer step for the n_{th} time, the Dragon Skin was relaxed sequentially until the L_0 was recovered. The size of the as-prepared MBGWF sensing film is 20×8 mm². Copper wires (2 μm in diameter) were connected to two ends of the as-prepared MBGWF with the assistance of silver paste. Here, ε_{sp} is the step pre-strain that controls the degree of the pre-strain and was determined according to the maximum sensing strain (ε_c) of the individual GWF sensing unit, ε_{pc} the step pre-cracking strain that controls the degree of pre-cracking, n the desired number of layers of GWFs stacked in the final strain sensor (e.g., $n = 10$ indicates 10-layer stacking of GWFs), L_0 the initial length of the substrate before stretched, and k (=1, 2, 3, ..., n) an integer indicating the number of repetitions that were carried out in the process, which also equals to the number of layers transferred in the process (e.g., $k = 3$ when the stated steps were repeated three times and three layers were transferred). See Table S5 for the specific value of each parameter for the MBGWF sensing film with $n = 1, 2, 3, 5$, and 10.

2.3. Characterization. The scanning electron microscopy (SEM), transmission electron microscopy (TEM), atomic force microscopy (AFM), and optical microscopy (OM) characterization were performed using the Hitachi SU8200 FE-SEM, JEM-2100F, Ntegra (NT-MDT), and Axio Lab.A1 (Carl Zeiss MicroImaging GmbH), respectively. The Raman testing was carried out using a DXR Raman Microscopy (Thermal Scientific Corporation, USA, with a 532 nm excitation length). In electromechanical tests, the relative resistance variation was acquired under various strain loading conditions (see Table S4 for details). The tensile strain loading was provided by a high-precision motorized linear stage (a displacement resolution of 2.5 μm, see Figure S1, Supporting Information for details on the sample fixation approach and device setup for tensile strain loading). A constant voltage (0.1 V) was loaded on the sensor using a two-point connection method to acquire a real-time current signal with an electrochemical workstation (PARSTAT 2273, Princeton Applied Research). Professional image analysis software Image-Pro-Plus 6 was used for the quantitative analysis of buckles and cracks (see Supporting Information for details).

3. RESULTS AND DISCUSSION

3.1. Fundamental Design Philosophy and Fabrication Process of the MBGWF Strain Sensor. We start with a discussion of the fundamental design philosophy. As shown in Figure 1a,b, n layers of sensing units with varying buckle wavelength are stacked to form the bulk sensing film, in which the buckle wavelength increases from the bottom layer to the top (flat layer, $\lambda \approx$ infinity). Understandably, when a specific sensing material with buckles is stretched, the applied strain will be accommodated by buckles such that the sensing material will not experience intrinsic strain that triggers the electrical response. In addition, the capability of the sensing material to accommodate the applied strain is highly dependent on the degree of buckling or the buckle wavelength. Because of the existence of the buckle wavelength gradient, when the bulk sensing film is loaded with strain, the top flat layer, without the aid of buckles, will first respond to stimuli, whereas underlayers remain unresponsive until their buckles disappear (λ reaches infinity). On the basis of the above analysis, if the buckle wavelength gradient is precisely controlled, we could reasonably expect interesting electromechanical behaviors of each sensing unit as depicted in Figure 1c. Here, we term the unresponsive state (blue part in Figure 1c) as the conducting mode, whereas the responsive one (red part) as the sensing mode. Specifically, underlayers will switch from their conducting mode to the sensing mode exactly when corresponding upper layers reach their strain sensing limit (ε_c). The direct result is that, ideally, multilayer sensing units will work cooperatively, as runners do in a relay race, to break the sensing limit of an individual and extend the overall strain sensing range to any desirable higher level. Meanwhile, high global sensitivity could also be acquired by carefully choosing a sufficiently sensitive sensing unit.

The crux lies in how to introduce such a through-layer buckle wavelength gradient into a sensing film composed of multi-layered sensing units. As a demonstration, the GWF was chosen as the sensing unit and Figure 1d,e schematically illustrates the fabrication strategy for the MBGWF strain sensor (see the Experimental Section for fabrication details). The process starts with the preparation of the free-standing GWF film on water following the method stated in a previous work.[38] Then, the Dragon Skin was prestretched to the length of $(\varepsilon_{sp} + 1)^{(n-1)}L_0$,
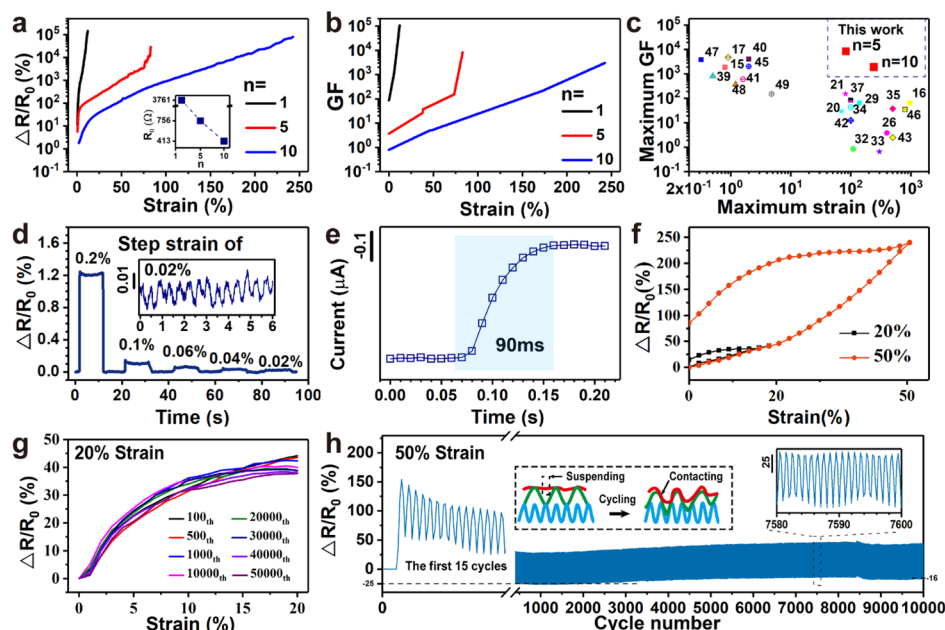
Figure 3. Electromechanical performances of MBGWF sensors. Plots of (a) relative resistance variation vs strain (the inset figure shows the initial resistances for varing n) and (b) GF vs strain for MBGWF strain sensors with varying n. (c) Summary of reported values of the maximum GF and the maximum sensing strain from the literature and results from this work. Relative resistance variation under (d) gradually diminishing step strain from 0.2 to 0.02% (the inset figure shows the response signal under the cyclic strain of 0.02%), (f) first stretching−releasing cycle at 20 and 50% strain, (g) cyclic strain of 20% (the starting resistance after k times of cycling tests was used for the value of R_0 to calculate $\Delta R/R_0$ for the kth curve), and (h) cyclic strain of 50% (the inset figures show the schematic illustration of the structural reconstruction process in the first 1000 cycles and the enlarged view of signals during 7580th−7600th cycles, respectively). (e) Current signal to a quasi-transient input step strain of 0.2%.

and the surface hydrophilicity was improved by applying the AP treatment (see Figure S6 for results of contact angle tests). Afterward, the as-prepared GWF was directly transferred onto the Dragon Skin from water, and the substrate was further stretched to the length of $(\varepsilon_{pc} + 1)(\varepsilon_{sp} + 1)^{(n-k)}L_0$ to precrack the as-transferred GWF and then relaxed to the length of $(\varepsilon_{sp} + 1)^{(n-k-1)}L_0$ to form buckles (see the Experimental Section for the definition of ε_{sp}, ε_{pc}, n, k, and L_0 and Figures 2a and S10 for the evolution of the morphology of a GWF following a cycle of the transfer, pre-cracking, and relaxing process). Last, by repeating transfer, pre-cracking, and relaxing $(n - 1)$ times and transfer for the last time (n_{th}), the Dragon Skin was relaxed sequentially until the initial length was recovered and we attained the MBGWF sensing film with n-layer stacking of selectively buckled GWFs (see Figure 1f for the photograph of the real sensor with $n = 10$ and Figure 1g for the cross-sectional SEM image of the MBGWF with $n = 3$).

Figure 2a shows that the as-prepared GWF film retained the woven structure of the copper mesh. After etching away the inner copper, the hollow structure collapsed into flattened GMRs (~140 μm in width) that interlaced with each other at right angles and formed square meshes of ~150 μm in width. The GWF was free-standing on water without the need of an intermediate substrate (Figure S7a,b). The Raman spectra suggest that the as-grown graphene is multilayered (>5 layers, see Figure S7d for detailed analysis). The thickness of a single-layer GMR was determined to be ~70 nm by the AFM (Figure S8). The electron diffraction pattern with a series of continuous hexagonal spots expected for graphene (Figure S9b) reveals the polycrystalline feature, which is further confirmed by distinguishable grain boundaries shown in dark-field TEM images (Figure S9c,d).

We also evaluated the mechanical properties of the bare Dragon Skin substrate and MBGWF strain sensors with different n values using tensile stress versus strain measurements (Figure 2d). The rupture strain of the Dragon Skin and sensors with $n = 1, 5, 10$ reached up to 590, 602, 612, and 616%, and the tensile strength was determined to be 1.14, 1.23, 1.17, and 1.17 MPa, respectively.

Figure 2b,e pictures the stacking and buckling condition of GWFs in MBGWF strain sensors with $n = 2$ and 3, respectively (see Figure S11 for images of the MBGWF sensing film with $n = 5$ and 10). Although the decreasing contrast among layers adds difficulties in distinguishing layer from layer, different layers could still be traced by scrutinizing differences in the buckling condition with the aid of the professional image analysis software (see Supporting Information for details on image analysis). In both cases, the lower layers are featured with buckles of smaller wavelength but higher distribution density. We measured the buckle wavelength of different layers for the sensor with $n = 3, 5$, and 10 using the professional image analysis software as stated before, and the result is presented in Figure 2c. Figure 2c clearly shows the formation of the buckle wavelength gradient through layers of different sensors. That is, the buckle wavelength increases from the bottom layer to the top layer. Note that the value of infinity was designated to the top layer arbitrarily because no pre-strain was applied to it. In short, such a sequential transfer-relaxing fabrication strategy introduced pre-strain of decreasing degree to each layer, which is effective in forming a through-layer buckle wavelength gradient.

3.2. Electromechanical Performances of the MBGWF Strain Sensor. Electromechanical performances of MBGWF strain sensors were investigated by recording the relative resistance variation ($\Delta R/R_0$) under various strain (ε) loading
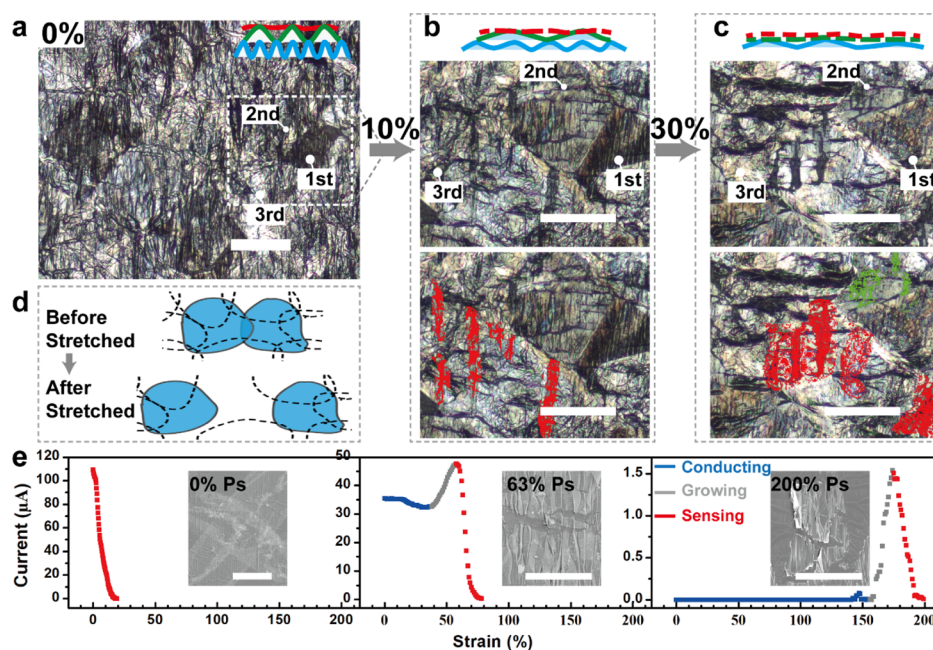
Figure 4. Illustration of the working mechanism of strain sensing. (a) OM image of the initial MBGWF strain sensor with $n = 3$ before stretching. The upper-right inset image shows the schematic illustration of the cross-sectional view of the sensing film. (b) Schematic illustration of the cross-sectional view of the sensing film under the strain of 10% (top), the enlarged OM image of the selected area in (a) under the strain of 10% (middle), and the corresponding colorized image (bottom). (c) Schematic illustration of the cross-sectional view of the sensing film under the strain of 30% (top), the enlarged OM image of the selected area in (a) under the strain of 30% (middle), and the corresponding colorized image (bottom). See Supporting Information for details on colorization and analysis of cracks. (d) Schematic illustration of the morphology evolution of the polycrystalline graphene under strain. (e) Plots of current vs strain for GWFs with 0, 63, and 200% pre-strain, respectively. Inset SEM images show the corresponding morphology before being stretched. Scale bar, 100 μm.

conditions. To determine the maximum strain sensing range and sensitivity, MBGWF sensors with varying n were stretched until the sensing film lost conductivity. Highly tunable sensing performances were observed from Figure 3a: $\Delta R/R_0$ versus ε curves of three MBGWF strain sensors with $n = 1$, 5, and 10 share the same exponential growth pattern whereas diverge significantly in the maximum sensing strain and sensitivity (GF, defined as the slope, or $\mathrm{d}(\Delta R/R_0)/\mathrm{d}\varepsilon$). Precisely, with the increase of n from 1 to 5 and 10, the maximum sensing range is extended remarkably from 12 to 82.84 and 242.74%, whereas the GF at a fixed strain drops. Further calculation of GF (Figure 3b) shows that GF of these three MBGWF strain sensors also increases exponentially from 87, 4, and 1 to 105 674, 8315, and 2996, respectively, and the average GF within the maximum sensing strain was calculated to be 12 052, 350 and 327, respectively (see Figure S13 and Tables S1 and S2 for details on the calculation). Note that, despite an ultrahigh sensitivity (GF up to 10^6), the single-layer GWF-based strain sensor without any special structure design previously reported[38] has a very narrow strain sensing range ($\sim$10%), which limits its application in monitoring full-range human activities, especially those inducing large deformation. In comparison, in this work, by introducing the buckle wavelength gradient to multilayered GWFs, the strain sensing range of MBGWF strain sensors with $n = 5$ and 10 is improved by 7 and 23 times, respectively. Although the improvement in stretchability is achieved at the sacrifice of the sensitivity to some extent, because of the ultrahigh sensitivity of individual GWF, the sensitivity of MBGWF strain sensors is still maintained at a desirable high level. As shown in Figure 3c, the incorporation of a wide strain sensing range and high GF enables MBGWF strain sensors ($n = 5$ and 10) to stand out when compared with those reported in

the previous work (see Table S6 for a more comprehensive comparison of strain sensing performance parameters, including sensitivity, stretchability, minimum detection limit, durability, response time, and linearity).[15−17,20,21,26,29,32−35,37,39−43,45−49]

To further evaluate the sensing performances of the MBGWF strain sensor, the sensor with $n = 10$ was chosen as the testing sample (through later sections unless otherwise specified) and critical sensing parameters including the minimum detection limit, response time, and cyclic repeatability were determined. The minimum detection limit was measured to be as low as 0.02% by applying a series of diminishing step strain and cyclic strain loading of 0.02% (Figure 3d). Such a low detection limit should be highly desirable for monitoring subtle signals in wearable applications. The sensor also exhibits a fast stimuli response of <90 ms (Figure 3e, see Supporting Information for details on the testing approach).

The stretching−releasing cyclic repeatability of the sensor was tested at the strain of 20 and 50%, respectively (see Figure S18 for the cyclic repeatability of the sensor with $n = 1$ and 5). Figure 3f shows the $\Delta R/R_0$ curves for the first cycle. The sensor experienced a larger irreversible $\Delta R/R_0$ change of 85% when the strain recovered to 0% in the case of 50% strain, compared with that of $\sim$15% in the case of 20% strain. However, the relative change of $\Delta R/R_0$ (defined as $\Delta R/R_0$ at the 0% strain divided by that at the maximum strain for each curve) is comparable in the two cases, which was calculated to be 36.6% (=15%/41%) in the case of 20% strain and 35.4% (=85%/240%) in the case of 50% strain. Such an irreversible change of $\Delta R/R_0$ in a stretching−releasing cycle is usually termed the hysteresis effect, which is a widely reported to exist in strain
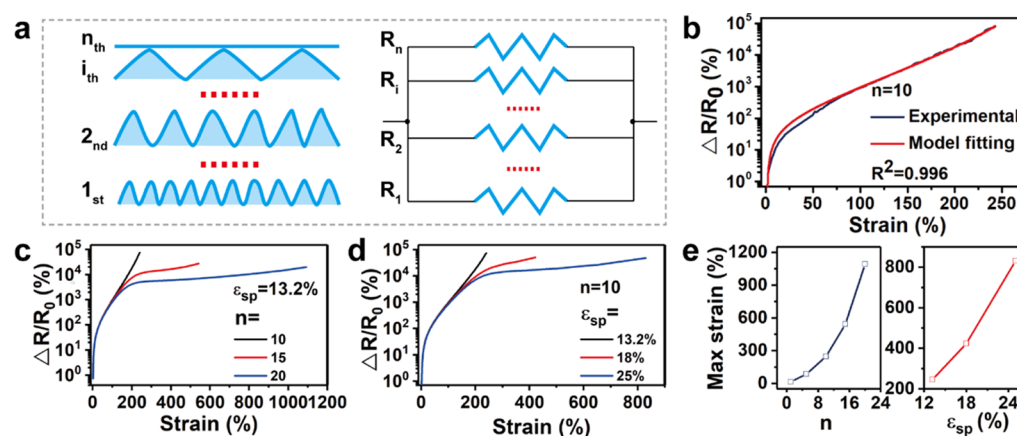
Figure 5. Modeling of strain sensing performances. (a) Schematic structure and electric circuit model of the n-layer MBGWF sensing film. R_i is the resistance corresponding to the ith sensing unit. (b) Modeling fitting of the relative resistance variation curve of the MBGWF strain sensor with n = 10. (c−e) Modeling prediction on the effect of fabrication parameters on the strain sensing performance. (c) Effect of repetition time n. (d) Effect of ε_{sp}. (e) Summary of the effect of n and ε_{sp} on the maximum sensing strain based on c−d.

sensors utilizing various sensing materials (graphene,[20] CB,[56] CNTs,[57,58] gold nanowires,[28] and silver nanowires[13]). Though still not very well understood, the hysteresis behavior could be attributed to the synergistic influence of the irreversible structural change and the interfacial interaction. Figure S14 shows the prolonged recording of the $\Delta R/R_0$ signal with a duration of 330 s after the strain recovering from 20 to 0%, from which we observed that a slow recovery process of the signal continued but the $\Delta R/R_0$ signal could not recover fully to 0%. The irreversible $\Delta R/R_0$ change could be due to the occurrence of the irreversible structural change, whereas the slow recovery process should be attributed to the viscoelastic nature of the Dragon Skin as a polymer elastomer[56,59−61] and potential sliding and friction between the substrate and the GWF and among the GWF sensing units.

Interestingly, in the subsequent cycling after the first cycle, a continued drop of the baseline of the $\Delta R/R_0$ curves occurs until 1000 cycles are finished (Figure 3h). To explore the reason for the initial drop of the baseline in the first 1000 cycles, we traced the morphology evolution of the sensing film with 10-layer GWFs, following a 50 000 time cycling test at the strain of 50% (Figure S15). Macrophotograph (Figure S15c) shows the decrease of flatness of the sensor surface with the increase of cycling number. OM images (Figure S15a′,a″,b′,b″) show that after 50 000 times of stretching−releasing cycling, the upper GWFs form a more conformal contact with lower layers, as indicated by the visible buckling configuration of lower layers. Such observations indicate that a structural reconstruction process occurred during the first 1000 cycles. That is, during the stretching−releasing process, the suspending part (the inset images of Figure 3h) of the upper layers should form a better contact with lower ones. Such a reconstruction process was facilitated by the increase of the cycle number until 1000 cycles. Understandably, a better contact among the layers should result in a better conductivity of the sensing film and thus the drop of the baseline of the $\Delta R/R_0$ curves.

As shown in Figure 3h, at the strain of 50%, the sensor works relatively stable through 1000 to 10 000 cycles, with only a slight increase of the baseline from −25% (1000th cycle) to −16% (10 000th cycle). At a cyclic loading of 20% strain (Figure 3g), compared with that after 100 cycles, the response curve remained nearly unchanged after 1000 cycles and

experienced a relative drift of −9.4 and −14.5% at the point of 20% strain after 10 000 and 50 000 cycles, respectively.

3.3. Working Mechanism and Modeling Study on Effects of Critical Parameters. Such highly tunable performances in the strain sensing range and sensitivity should be a desirable result benefiting from both ultrasensitivity of the GWF sensing unit and the through-layer buckle wavelength gradient. For one thing, similar to other sensing materials based on the cracking mechanism,[34,62−64] the GWF sensing unit possesses an ultrahigh sensitivity to strain. As mentioned before, the as-prepared graphene for the individual GWF has a polycrystalline feature composed of overlapped graphene domains (Figure 4d). Under a strain loading, cracks initiate and propagate as a result of relative sliding among adjacent graphene domains, leading to a dramatic reduction of the conductive paths and thus giant electrical resistance variations.[38,65]

For the other, the morphology evolution of the MBGWF strain sensors with n = 3 and n = 10 under a series of stretching conditions (Figures 4a−c and S12) reveals that the through-layer buckle wavelength gradient leads to a layer-by-layer cracking process, accounting for the working mechanism of the MBGWF strain sensor. For clarity, the case of n = 3 was selected for the following discussion. Figure 4a shows the stacking and buckling condition of layers as stated before. Under the strain of 10% (Figure 4b), cracks perpendicular to the direction of stretching (marked as red in Figure 4b) initiated on the third layer but was not observed on the first and second layer. Instead, both the first and second layer accommodated applied strain through the increase of buckle wavelength. As the strain was increased to 30% (Figure 4c), cracks on the third layer tended to widen (marked as red in Figure 4c). Meanwhile, buckles on the second layer were also replaced by cracks (marked as green in Figure 4c) that were narrower than those on the third layer, and the first layer still retained buckles with further increasing wavelength. Clearly, the buckle wavelength gradient endowed different layers with varying capability of accommodating strain thus enabling cracks to propagate through layers in a controllable time-delayed manner (see inset images in Figure 4a−c for the schematic illustration of the cross-sectional evolution).

Such a layer-by-layer cracking process further leads to a layer-by-layer electrical signal response. Figure 4e shows how varying
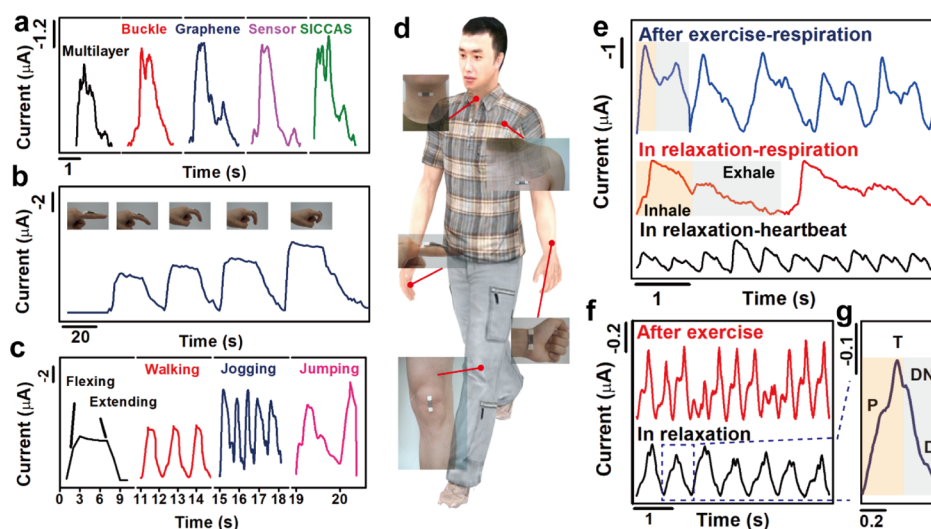
Figure 6. Demonstration of monitoring full-range human activities. (d) Schematic illustration of a human body and photographs showing the sensor attached to various parts. Responsive current signals of the sensor attached to (a) throat when the wearer spoke various words, (b) finger in a bending process, (c) knee under various motions, (e) breast when the wearer was in relaxation and after exercise, and (f) wrist when the wearer was in relaxation and after exercise. (g) Enlarged view of an individual pulse contour selected from (f) (systolic and diastolic activity was marked as pink and blue, respectively). A constant voltage of 0.1 V was applied in all cases.

buckle wavelength created by different pre-strain conditions influences the sensing behavior of the individual GWF. In the case of the GWF applied with 0% pre-strain, the sensing mode (marked as red in Figure 4e) starts immediately when stretched. In comparison, in the case of the GWF with 63 and 200% pre-strain, the starting point of the sensing mode shifts remarkably from 0 to 58 and 174%, respectively. Interestingly, apart from conducting (marked as blue in Figure 4e) and sensing mode as expected, a growing mode (marked as gray in Figure 4e) was also observed, which should be attributed to the recontact of parallel cracks (see Figure S16 for detailed analysis). Here, we see that the buckle plays the role as a "switch" that controls the on−off state of the sensing mode of individual sensing units. Liu et al.[21] also utilized the prestretching approach in the design of the so-called FSG sensor, which has a fish-scale-like structure formed by overlapped bilayer rGO. Working based on the separation of the overlapped bilayer rGO, the FSG sensor has a quite wide strain sensing range of ∼82% and a high GF of 16.2 to 150. However, on the basis of the above analysis, the working mechanism of our MBGWF sensor differs greatly from that of the FSG sensor. That is, the through-layer buckle wavelength gradient enables multilayer sensing units to work cooperatively to break the maximum sensing limit of an individual and extend it to a desirable higher level.

On the basis of this layer-by-layer cracking mechanism, we further developed a simplified model to investigate how fabrication parameters affect electromechanical performances of the MBGWF strain sensor (details on the derivation process and corresponding schematic illustrations are provided in the Supporting Information and Figures S2−S4). Briefly, we established an electric circuit regarding the stacked n-layer GWFs inside the MBGWF film as n resistors (R_i) in parallel (Figure 5a). Through critical derivation, we arrived at a set of equations (eqs S5, S8, S22, S28, and S21) describing the relation between the overall relative resistance variation ($\Delta R/R_0$) and the overall strain (ε). These equations were applied to fit the experimentally determined $\Delta R/R_0$ versus ε curve of the MBGWF strain sensor with $n = 10$ (see Table S3 for details on

fitting results). Figure 5b shows a high degree of fitting ($R^2 = 0.996$), which validates the accuracy of the layer-by-layer cracking mechanism.

This layer-by-layer cracking model was found to be useful in prediction of the effect of fabrication parameters on electromechanical performances of the MBGWF strain sensor (Figure 5c−e). Interestingly, the repetition time (n) and the step pre-strain (ε_{sp}) share a similar effect on the trend of the $\Delta R/R_0$ versus ε curve. That is, with the increase of each parameter, the maximum sensing strain could be improved, whereas the slope (or the sensitivity) could be lowered.

The effect of n predicted by modeling (Figure 5c) coincides well with the experimental results (Figure 3a). Notably, the predicted maximum sensing strain could be higher than 500 and 1000% with $n = 15$ and 20, respectively (Figure 5c,e). Such a result becomes understandable when we recall that the increase in the repetition time immediately adds new layers to the sensing film, which will widen the strain limit through the layer-by-layer cracking mechanism as discussed. Besides, adjusting ε_{sp} was also proved to be an effective way of modifying the maximum sensing strain (Figure 5d,e). An increase of ε_{sp} from 13.2 to 18 and 25% will widen the maximum sensing strain to more than 400 and 800%, respectively. Such findings clearly suggest the high adjustability of sensing performances of the MBGWF strain sensor. In addition, if we could overcome some practical difficulties, such as the limit of stretchability of the substrate, the strain sensing range could be freely extended to a higher level.

In our design, to guarantee that the sensing mode of a lower layer will immediately start when a higher layer reaches its ε_c, ε_{sp} was carefully controlled to equal to ε_c of each sensing unit. Thus, any parameters that affect ε_c of the individual GWF will, in turn, determine the overall performance of the strain sensor. Further tests (Figure S17a,b) show that the stretching angle (defined as the included angle between the GMR and the stretching direction) and pre-cracking are two parameters that strongly influence the electromechanical performance of the individual GWF. Briefly, on one hand, stretching in 45° will result in a higher ε_c but lower sensitivity compared with 0°. On

the other hand, pre-cracking of the GWF will enhance the sensitivity of the GWF but lower the ε_c. In addition, the combination of a stretching angle of 45° and pre-cracking was proved to be the optimal condition for the MBGWF strain sensor to achieve a balanced ε_c and sensitivity (Figure S17c). This is the reason why the stretching angle was controlled to be 45° in the transfer process and the pre-cracking step was included in the fabrication of the sensors.

3.4. Capability of Monitoring Full-Range Human Activities. To demonstrate the promising potential of the MBGWF strain sensor as a wearable sensor for monitoring the full-range human activities, we attached the sensor to various parts of a human body with the help of a medical tape (Figure 6d). For one thing, the high stretchability allows the sensor in monitoring vigorous joint motions. Figure 6b shows stable step signals responding to the finger motions. In addition, various knee-related activities such as flexing/extending, walking, jogging, and jumping could be clearly distinguished by the difference in their amplitude and frequency (Figure 6c).

For the other, the strain sensor shows the advantage of high sensitivity and fast response in sensing subtle physical signals. As shown in Figure 6a, the sensor could effectively respond to subtle stimuli of complicated epidermis/muscle movements around the throat during phonation and recognize different patterns of relatively long words such as "multilayer", "buckle", "graphene", "sensor", and "SICCAS", which implies a great potential in applications such as speech rehabilitation training and human/machine interaction.[34,66] Besides, the capability of monitoring subtle physiological signals is also of great importance for disease diagnosis and personal health care. Figure 6e shows that muscle movements in the chest caused by respiration could be well-recorded by the sensor and variations in depth and rate of the respiration before and after exercise were clearly distinguished. Interestingly, because of high sensitivity and fast response of the sensor, the contribution of the heartbeat was also recorded in the form of subpeaks in the signal for respiration. Wrist pulse is another key indicator of one's health condition, providing useful information on arterial blood pressure and heart rate.[67,68] Figure 6f shows that a male in relaxation had a pulse frequency of 85 beat min^{-1}, which was accelerated to 120 beat min^{-1} after exercise, accompanied by strengthening in intensity. Apart from the pulse rate and intensity, accurate disease diagnosis relies on more detailed information on the pulse contours. A closer inspection on an individual pulse contour (Figure 6g) shows that it is composed of four characteristic subpeaks traditionally termed percussion wave (P), tidal wave (T), dicrotic notch (DN), and diastolic wave (D). DN divides the pulse into two parts corresponding to the systolic (pink in Figure 6g) and diastolic (blue in Figure 6g) activity. As for the underlying mechanism for such subpeaks, it is widely accepted that the P-wave is the result of the impulse generated by ventricular ejection, whereas diverse explanations exist for T-wave, DN, and D-wave.[69] Despite such inconsistency, we could still conclude that such a high-resolution pulse signal with detailed clinical messages should be desired by continuous and noninvasive pulse monitoring and disease diagnosis.

4. CONCLUSIONS

To sum up, we presented a through-layer buckle wavelength-gradient design and a facile and universal strategy for introducing the gradient into multilayered sensing units. Following this design, strain sensors using GWFs as sensing units exhibit highly tunable electromechanical performances and a desirable incorporation of high sensitivity and stretchability, ultralow detection limit, a fast signal response, and a high cyclic durability. Moreover, the promising potential of the MBGWF strain sensor as the wearable sensor was demonstrated by its excellent performances in the full-range human activities. A series of critical observations revealed the underlying working mechanism to be a layer-by-layer cracks propagation and response. In addition, the modeling study predicted influences of critical parameters on sensing performances. Also, such a facile strategy could be immediately adapted by replacing the sensing unit with alternative materials, giving rise to the promising potential for further tuning the sensing properties that meet requirements of emerging applications.

■ ASSOCIATED CONTENT

ⓢ Supporting Information

The Supporting Information is available free of charge on the ACS Publications website at DOI: 10.1021/acsami.7b17975.

> Extra details on methods, modeling derivation, complete characterization data, fitting and calculation of GFs, and complementary testing on sensing performances (PDF)

■ AUTHOR INFORMATION

Corresponding Authors
*E-mail: wangranran@mail.sic.ac.cn (R.W.).
*E-mail: jingsun@mail.sic.ac.cn (J.S.).
ORCID ⓞ
Jing Sun: 0000-0003-1101-1584
Notes
The authors declare no competing financial interest.

■ REFERENCES

(1) Tee, B. C.-K.; Chortos, A.; Berndt, A.; Nguyen, A. K.; Tom, A.; McGuire, A.; Lin, Z. C.; Tien, K.; Bae, W.-G.; Wang, H. A Skin-Inspired Organic Digital Mechanoreceptor. *Science* **2015**, *350*, 313−316.

(2) Yokota, T.; Zalar, P.; Kaltenbrunner, M.; Jinno, H.; Matsuhisa, N.; Kitanosako, H.; Tachibana, Y.; Yukita, W.; Koizumi, M.; Someya, T. Ultraflexible Organic Photonic Skin. *Sci. Adv.* **2016**, *2*, No. e1501856.

(3) Lim, S.; Son, D.; Kim, J.; Lee, Y. B.; Song, J.-K.; Choi, S.; Lee, D. J.; Kim, J. H.; Lee, M.; Hyeon, T.; Kim, D.-H. Transparent and Stretchable Interactive Human Machine Interface Based on Patterned Graphene Heterostructures. *Adv. Funct. Mater.* **2015**, *25*, 375−383.

(4) Wang, C.; Hwang, D.; Yu, Z.; Takei, K.; Park, J.; Chen, T.; Ma, B.; Javey, A. User-Interactive Electronic Skin for Instantaneous Pressure Visualization. *Nat. Mater.* **2013**, *12*, 899−904.

(5) Son, D.; Lee, J.; Qiao, S.; Ghaffari, R.; Kim, J.; Lee, J. E.; Song, C.; Kim, S. J.; Lee, D. J.; Jun, S. W.; Yang, S.; Park, M.; Shin, J.; Do, K.; Lee, M.; Kang, K.; Hwang, C. S.; Lu, N.; Hyeon, T.; Kim, D.-H. Multifunctional Wearable Devices for Diagnosis and Therapy of Movement Disorders. *Nat. Nanotechnol.* **2014**, *9*, 397−404.

(6) Koo, J. H.; Jeong, S.; Shim, H. J.; Son, D.; Kim, J.; Kim, D. C.; Choi, S.; Hong, J.-I.; Kim, D.-H. Wearable Electrocardiogram Monitor

Using Carbon Nanotube Electronics and Color-Tunable Organic Light-Emitting Diodes. *ACS Nano* **2017**, *11*, 10032−10041.

(7) Webb, R. C.; Bonifas, A. P.; Behnaz, A.; Zhang, Y.; Yu, K. J.; Cheng, H.; Shi, M.; Bian, Z.; Liu, Z.; Kim, Y.-S.; Yeo, W.-H.; Park, J. S.; Song, J.; Li, Y.; Huang, Y.; Gorbach, A. M.; Rogers, J. A. Ultrathin Conformal Devices for Precise and Continuous Thermal Characterization of Human Skin. *Nat. Mater.* **2013**, *12*, 938−944.

(8) Webb, R. C.; Ma, Y.; Krishnan, S.; Li, Y.; Yoon, S.; Guo, X.; Feng, X.; Shi, Y.; Seidel, M.; Cho, N. H. Epidermal Devices for Noninvasive, Precise, and Continuous Mapping of Macrovascular and Microvascular Blood Flow. *Sci. Adv.* **2015**, *1*, No. e1500701.

(9) Zhao, S.; Li, J.; Cao, D.; Zhang, G.; Li, J.; Li, K.; Yang, Y.; Wang, W.; Jin, Y.; Sun, R.; Wong, C.-P. Recent Advancements in Flexible and Stretchable Electrodes for Electromechanical Sensors: Strategies, Materials, and Features. *ACS Appl. Mater. Interfaces* **2017**, *9*, 12147−12164.

(10) Lee, J.; Kim, S.; Lee, J.; Yang, D.; Park, B. C.; Ryu, S.; Park, I. A Stretchable Strain Sensor Based on a Metal Nanoparticle Thin Film for Human Motion Detection. *Nanoscale* **2014**, *6*, 11932−11939.

(11) Zheng, M.; Li, W.; Xu, M.; Xu, N.; Chen, P.; Han, M.; Xie, B. Strain Sensors Based on Chromium Nanoparticle Arrays. *Nanoscale* **2014**, *6*, 3930−3933.

(12) Amjadi, M.; Pichitpajongkit, A.; Lee, S.; Ryu, S.; Park, I. Highly Stretchable and Sensitive Strain Sensor Based on Silver Nanowire-Elastomer Nanocomposite. *ACS Nano* **2014**, *8*, 5154−5163.

(13) Lee, H.; Seong, B.; Moon, H.; Byun, D. Directly Printed Stretchable Strain Sensor Based on Ring and Diamond Shaped Silver Nanowire Electrodes. *RSC Adv.* **2015**, *5*, 28379−28384.

(14) Xiao, X.; Yuan, L.; Zhong, J.; Ding, T.; Liu, Y.; Cai, Z.; Rong, Y.; Han, H.; Zhou, J.; Wang, Z. L. High-Strain Sensors Based on Zno Nanowire/Polystyrene Hybridized Flexible Films. *Adv. Mater.* **2011**, *23*, 5440−5444.

(15) Zhang, W.; Zhu, R.; Nguyen, V.; Yang, R. Highly Sensitive and Flexible Strain Sensors Based on Vertical Zinc Oxide Nanowire Arrays. *Sens. Actuators, A* **2014**, *205*, 164−169.

(16) Ryu, S.; Lee, P.; Chou, J. B.; Xu, R.; Zhao, R.; Hart, A. J.; Kim, S.-G. Extremely Elastic Wearable Carbon Nanotube Fiber Strain Sensor for Monitoring of Human Motion. *ACS Nano* **2015**, *9*, 5929−5936.

(17) Song, Y.; Lee, J.-I.; Pyo, S.; Eun, Y.; Choi, J.; Kim, J. A Highly Sensitive Flexible Strain Sensor Based on the Contact Resistance Change of Carbon Nanotube Bundles. *Nanotechnology* **2016**, *27*, 205502.

(18) Hu, C.; Li, Z.; Wang, Y.; Gao, J.; Dai, K.; Zheng, G.; Liu, C.; Shen, C.; Song, H.; Guo, Z. Comparative Assessment of the Strain-Sensing Behaviors of Polylactic Acid Nanocomposites: Reduced Graphene Oxide or Carbon Nanotubes. *J. Mater. Chem. C* **2017**, *5*, 2318−2328.

(19) Wang, N.; Xu, Z.; Zhan, P.; Dai, K.; Zheng, G.; Liu, C.; Shen, C. A Tunable Strain Sensor Based on a Carbon Nanotubes/Electrospun Polyamide 6 Conductive Nanofibrous Network Embedded into Poly(Vinyl Alcohol) with Self-Diagnosis Capabilities. *J. Mater. Chem. C* **2017**, *5*, 4408−4418.

(20) Jeong, Y. R.; Park, H.; Jin, S. W.; Hong, S. Y.; Lee, S.-S.; Ha, J. S. Highly Stretchable and Sensitive Strain Sensors Using Fragmentized Graphene Foam. *Adv. Funct. Mater.* **2015**, *25*, 4228−4236.

(21) Liu, Q.; Chen, J.; Li, Y.; Shi, G. High-Performance Strain Sensors with Fish-Scale-Like Graphene-Sensing Layers for Full-Range Detection of Human Motions. *ACS Nano* **2016**, *10*, 7901−7906.

(22) Wang, Y.; Hao, J.; Huang, Z.; Zheng, G.; Dai, K.; Liu, C.; Shen, C. Flexible Electrically Resistive-Type Strain Sensors Based on Reduced Graphene Oxide-Decorated Electrospun Polymer Fibrous Mats for Human Motion Monitoring. *Carbon* **2018**, *126*, 360−371.

(23) Li, X.; Yang, T.; Yang, Y.; Zhu, J.; Li, L.; Alam, F. E.; Li, X.; Wang, K.; Cheng, H.; Lin, C.-T.; Fang, Y.; Zhu, H. Large-Area Ultrathin Graphene Films by Single-Step Marangoni Self-Assembly for Highly Sensitive Strain Sensing Application. *Adv. Funct. Mater.* **2016**, *26*, 1322−1329.

(24) Shi, J.; Li, X.; Cheng, H.; Liu, Z.; Zhao, L.; Yang, T.; Dai, Z.; Cheng, Z.; Shi, E.; Yang, L.; Zhang, Z.; Cao, A.; Zhu, H.; Fang, Y. Graphene Reinforced Carbon Nanotube Networks for Wearable Strain Sensors. *Adv. Funct. Mater.* **2016**, *26*, 2078−2084.

(25) Mattmann, C.; Clemens, F.; Tröster, G. Sensor for Measuring Strain in Textile. *Sensors* **2008**, *8*, 3719−3732.

(26) Muth, J. T.; Vogt, D. M.; Truby, R. L.; Mengüç, Y.; Kolesky, D. B.; Wood, R. J.; Lewis, J. A. Embedded 3d Printing of Strain Sensors within Highly Stretchable Elastomers. *Adv. Mater.* **2014**, *26*, 6307−6312.

(27) Shin, U.-H.; Jeong, D.-W.; Park, S.-M.; Kim, S.-H.; Lee, H. W.; Kim, J.-M. Highly Stretchable Conductors and Piezocapacitive Strain Gauges Based on Simple Contact-Transfer Patterning of Carbon Nanotube Forests. *Carbon* **2014**, *80*, 396−404.

(28) Gong, S.; Lai, D. T. H.; Su, B.; Si, K. J.; Ma, Z.; Yap, L. W.; Guo, P.; Cheng, W. Highly Stretchy Black Gold E-Skin Nanopatches as Highly Sensitive Wearable Biomedical Sensors. *Adv. Electron. Mater.* **2015**, *1*, 1400063.

(29) Amjadi, M.; Yoon, Y. J.; Park, I. Ultra-Stretchable and Skin-Mountable Strain Sensors Using Carbon Nanotubes-Ecoflex Nanocomposites. *Nanotechnology* **2015**, *26*, 375501.

(30) Yamada, T.; Hayamizu, Y.; Yamamoto, Y.; Yomogida, Y.; Izadi-Najafabadi, A.; Futaba, D. N.; Hata, K. A Stretchable Carbon Nanotube Strain Sensor for Human-Motion Detection. *Nat. Nanotechnol.* **2011**, *6*, 296−301.

(31) Cai, L.; Song, L.; Luan, P.; Zhang, Q.; Zhang, N.; Gao, Q.; Zhao, D.; Zhang, X.; Tu, M.; Yang, F.; Zhou, W.; Fan, Q.; Luo, J.; Zhou, W.; Ajayan, P. M.; Xie, S. Super-Stretchable, Transparent Carbon Nanotube-Based Capacitive Strain Sensors for Human Motion Detection. *Sci. Rep.* **2013**, *3*, 3048.

(32) Yu, G.-F.; Yan, X.; Yu, M.; Jia, M.-Y.; Pan, W.; He, X.-X.; Han, W.-P.; Zhang, Z.-M.; Yu, L.-W.; Long, Y.-Z. Patterned, Highly Stretchable and Conductive Nanofibrous Pani/Pvdf Strain Sensors Based on Electrospinning and in Situ Polymerization. *Nanoscale* **2016**, *8*, 2944−2950.

(33) Wang, Z.; Huang, Y.; Sun, J.; Huang, Y.; Hu, H.; Jiang, R.; Gai, W.; Li, G.; Zhi, C. Polyurethane/Cotton/Carbon Nanotubes Core-Spun Yarn as High Reliability Stretchable Strain Sensor for Human Motion Detection. *ACS Appl. Mater. Interfaces* **2016**, *8*, 24837−24843.

(34) Kang, D.; Pikhitsa, P. V.; Choi, Y. W.; Lee, C.; Shin, S. S.; Piao, L.; Park, B.; Suh, K.-Y.; Kim, T.-i.; Choi, M. Ultrasensitive Mechanical Crack-Based Sensor Inspired by the Spider Sensory System. *Nature* **2014**, *516*, 222−226.

(35) Wu, J. M.; Chen, C.-Y.; Zhang, Y.; Chen, K.-H.; Yang, Y.; Hu, Y.; He, J.-H.; Wang, Z. L. Ultrahigh Sensitive Piezotronic Strain Sensors Based on a Znsno3 Nanowire/Microwire. *ACS Nano* **2012**, *6*, 4369−4374.

(36) Liao, Q.; Mohr, M.; Zhang, X.; Zhang, Z.; Zhang, Y.; Fecht, H.-J. Carbon Fiber-Zno Nanowire Hybrid Structures for Flexible and Adaptable Strain Sensors. *Nanoscale* **2013**, *5*, 12350−12355.

(37) Fu, X.-W.; Liao, Z.-M.; Zhou, J.-X.; Zhou, Y.-B.; Wu, H.-C.; Zhang, R.; Jing, G.; Xu, J.; Wu, X.; Guo, W.; Yu, D. Strain Dependent Resistance in Chemical Vapor Deposition Grown Graphene. *Appl. Phys. Lett.* **2011**, *99*, 213107.

(38) Li, X.; Zhang, R.; Yu, W.; Wang, K.; Wei, J.; Wu, D.; Cao, A.; Li, Z.; Cheng, Y.; Zheng, Q.; Ruoff, R. S.; Zhu, H. Stretchable and Highly Sensitive Graphene-on-Polymer Strain Sensors. *Sci. Rep.* **2012**, *2*, 870.

(39) Zhao, J.; Wang, G.; Yang, R.; Lu, X.; Cheng, M.; He, C.; Xie, G.; Meng, J.; Shi, D.; Zhang, G. Tunable Piezoresistivity of Nanographene Films for Strain Sensing. *ACS Nano* **2015**, *9*, 1622−1629.

(40) Liu, N.; Fang, G.; Wan, J.; Zhou, H.; Long, H.; Zhao, X. Electrospun Pedot:Pss-Pva Nanofiber Based Ultrahigh-Strain Sensors with Controllable Electrical Conductivity. *J. Mater. Chem.* **2011**, *21*, 18962−18966.

(41) Lee, T.; Choi, Y. W.; Lee, G.; Pikhitsa, P. V.; Kang, D.; Kim, S. M.; Choi, M. Transparent Ito Mechanical Crack-Based Pressure and Strain Sensor. *J. Mater. Chem. C* **2016**, *4*, 9947−9953.

(42) Liao, X.; Zhang, Z.; Liao, Q.; Liang, Q.; Ou, Y.; Xu, M.; Li, M.; Zhang, G.; Zhang, Y. Flexible and Printable Paper-Based Strain

Sensors for Wearable and Large-Area Green Electronics. *Nanoscale* **2016**, *8*, 13025−13032.

(43) Hwang, B.-U.; Lee, J.-H.; Tran Quang, T.; Roh, E.; Kim, D.-I.; Kim, S.-W.; Lee, N.-E. Transparent Stretchable Self-Powered Patchable Sensor Platform with Ultrasensitive Recognition of Human Activities. *ACS Nano* **2015**, *9*, 8801−8810.

(44) Roh, E.; Hwang, B.-U.; Kim, D.; Kim, B.-Y.; Lee, N.-E. Stretchable, Transparent, Ultrasensitive, and Patchable Strain Sensor for Human/Machine Interfaces Comprising a Nanohybrid of Carbon Nanotubes and Conductive Elastomers. *ACS Nano* **2015**, *9*, 6252−6261.

(45) Boland, C. S.; Khan, U.; Backes, C.; O'Neill, A.; McCauley, J.; Duane, S.; Shanker, R.; Liu, Y.; Jurewicz, I.; Dalton, A. B.; Coleman, J. N. Sensitive, High-Strain, High-Rate Bodily Motion Sensors Based on Graphene-Rubber Composites. *ACS Nano* **2014**, *8*, 8819−8830.

(46) Wang, S.; Zhang, X.; Wu, X.; Lu, C. Tailoring Percolating Conductive Networks of Natural Rubber Composites for Flexible Strain Sensors Via a Cellulose Nanocrystal Templated Assembly. *Soft Matter* **2016**, *12*, 845−852.

(47) Wang, C.; Li, X.; Gao, E.; Jian, M.; Xia, K.; Wang, Q.; Xu, Z.; Ren, T.; Zhang, Y. Carbonized Silk Fabric for Ultrastretchable, Highly Sensitive, and Wearable Strain Sensors. *Adv. Mater.* **2016**, *28*, 6640−6648.

(48) Lin, Y.; Liu, S.; Chen, S.; Wei, Y.; Dong, X.; Liu, L. A Highly Stretchable and Sensitive Strain Sensor Based on Graphene-Elastomer Composites with a Novel Double-Interconnected Network. *J. Mater. Chem. C* **2016**, *4*, 6345−6352.

(49) Zhang, M.; Wang, C.; Wang, H.; Jian, M.; Hao, X.; Zhang, Y. Carbonized Cotton Fabric for High-Performance Wearable Strain Sensors. *Adv. Funct. Mater.* **2017**, *27*, 1604795.

(50) Yin, B.; Wen, Y.; Hong, T.; Xie, Z.; Yuan, G.; Ji, Q.; Jia, H. Highly Stretchable, Ultrasensitive, and Wearable Strain Sensors Based on Facilely Prepared Reduced Graphene Oxide Woven Fabrics in an Ethanol Flame. *ACS Appl. Mater. Interfaces* **2017**, *9*, 32054−32064.

(51) Liu, Z.; Meyers, M. A.; Zhang, Z.; Ritchie, R. O. Functional Gradients and Heterogeneities in Biological Materials: Design Principles, Functions, and Bioinspired Applications. *Prog. Mater. Sci.* **2017**, *88*, 467−498.

(52) Peisker, H.; Michels, J.; Gorb, S. N. Evidence for a Material Gradient in the Adhesive Tarsal Setae of the Ladybird Beetle Coccinella Septempunctata. *Nat. Commun.* **2013**, *4*, 1661.

(53) Gorb, S. N.; Beutel, R. G.; Gorb, E. V.; Jiao, Y.; Kastner, V.; Niederegger, S.; Popov, V. L.; Scherge, M.; Schwarz, U.; Vötsch, W. Structural Design and Biomechanics of Friction-Based Releasable Attachment Devices in Insects. *Integr. Comp. Biol.* **2002**, *42*, 1127−1139.

(54) Tan, Y.; Hoon, S.; Guerette, P. A.; Wei, W.; Ghadban, A.; Hao, C.; Miserez, A.; Waite, J. H. Infiltration of Chitin by Protein Coacervates Defines the Squid Beak Mechanical Gradient. *Nat. Chem. Biol.* **2015**, *11*, 488−495.

(55) Miserez, A.; Schneberk, T.; Sun, C.; Zok, F. W.; Waite, J. H. The Transition from Stiff to Compliant Materials in Squid Beaks. *Science* **2008**, *319*, 1816−1819.

(56) Pang, C.; Lee, G.-Y.; Kim, T.-i.; Kim, S. M.; Kim, H. N.; Ahn, S.-H.; Suh, K.-Y. A Flexible and Highly Sensitive Strain-Gauge Sensor Using Reversible Interlocking of Nanofibres. *Nat. Mater.* **2012**, *11*, 795−801.

(57) Liu, C.-X.; Choi, J.-W. Analyzing Resistance Response of Embedded Pdms and Carbon Nanotubes Composite under Tensile Strain. *Microelectron. Eng.* **2014**, *117*, 1−7.

(58) Zhang, R.; Deng, H.; Valenca, R.; Jin, J.; Fu, Q.; Bilotti, E.; Peijs, T. Strain Sensing Behaviour of Elastomeric Composite Films Containing Carbon Nanotubes under Cyclic Loading. *Compos. Sci. Technol.* **2013**, *74*, 1−5.

(59) Kim, T. K.; Kim, J. K.; Jeong, O. C. Measurement of Nonlinear Mechanical Properties of Pdms Elastomer. *Microelectron. Eng.* **2011**, *88*, 1982−1985.

(60) Amjadi, M.; Kyung, K.-U.; Park, I.; Sitti, M. Stretchable, Skin-Mountable, and Wearable Strain Sensors and Their Potential Applications: A Review. *Adv. Funct. Mater.* **2016**, *26*, 1678−1698.

(61) Fan, Q.; Qin, Z.; Gao, S.; Wu, Y.; Pionteck, J.; Maeder, E.; Zhu, M. The Use of a Carbon Nanotube Layer on a Polyurethane Multifilament Substrate for Monitoring Strains as Large as 400%. *Carbon* **2012**, *50*, 4085−4092.

(62) Zhao, S.; Guo, L.; Li, J.; Li, N.; Zhang, G.; Gao, Y.; Li, J.; Cao, D.; Wang, W.; Jin, Y.; Sun, R.; Wong, C. P. Binary Synergistic Sensitivity Strengthening of Bioinspired Hierarchical Architectures Based on Fragmentized Reduced Graphene Oxide Sponge and Silver Nanoparticles for Strain Sensors and Beyond. *Small* **2017**, *13*, 1700944.

(63) Han, F.; Li, J.; Zhao, S.; Zhang, Y.; Huang, W.; Zhang, G.; Sun, R.; Wong, C.-P. A Crack-Based Nickel@Graphene-Wrapped Polyurethane Sponge Ternary Hybrid Obtained by Electrodeposition for Highly Sensitive Wearable Strain Sensors. *J. Mater. Chem. C* **2017**, *5*, 10167−10175.

(64) Zhao, S.; Li, J.; Cao, D.; Gao, Y.; Huang, W.; Zhang, G.; Sun, R.; Wong, C.-P. Percolation Threshold-Inspired Design of Hierarchical Multiscale Hybrid Architectures Based on Carbon Nanotubes and Silver Nanoparticles for Stretchable and Printable Electronics. *J. Mater. Chem. C* **2016**, *4*, 6666−6674.

(65) Wang, W.; Yang, T.; Zhu, H.; Zheng, Q. Bio-Inspired Mechanics of Highly Sensitive Stretchable Graphene Strain Sensors. *Appl. Phys. Lett.* **2015**, *106*, 171903.

(66) Wang, X.; Gu, Y.; Xiong, Z.; Cui, Z.; Zhang, T. Silk-Molded Flexible, Ultrasensitive, and Highly Stable Electronic Skin for Monitoring Human Physiological Signals. *Adv. Mater.* **2014**, *26*, 1336−1342.

(67) O'Rourke, M. F.; Gallagher, D. E. Pulse Wave Analysis. *J. Hypertens.* **1996**, *14*, S147−S158.

(68) Marcinkevics, Z.; Greve, M.; Aivars, J. I.; Erts, R.; Zehtabi, A. H. Relationship between Arterial Pressure and Pulse Wave Velocity Using Photoplethysmography During the Post-Exercise Recovery Period. *Acta Univ. Latv.* **2009**, *753*, 59−68.

(69) O'Rourke, M. F. The Arterial Pulse in Health and Disease. *Am. Heart J.* **1971**, *82*, 687−702.